Two-Step Cavitation-Enhanced Waterborne CO_2 Management: Aqueous Capture via Electrospun Membranes and Controlled Hydrodynamic Release

Rokhsareh Bakhtiari[a,b], Seyedreza Tebyani[a,b], Araz Sheibani Aghdam[a,b], Mohammad Imanzadeh[a,b], Hongwei Wu[d], Ali Koşar[a,b,c], Morteza Ghorbani[a,b,c] and Fevzi Çakmak Cebeci[a,b,*]

[a]*Faculty of Engineering and Natural Science, Sabanci University, , Istanbul, 34956, Turkey*
[b]*SUNUM Nanotechnology Research Center, Sabanci University, , Istanbul, 34956, Turkey*
[c]*Center of Excellence for Functional Surfaces and Interfaces for Nano-Diagnostics (EFSUN), Sabanci University, , Istanbul, 34956, Turkey*
[d]*School of Physics, Engineering and Computer Science, University of Hertfordshire, , Hatfield, AL10 9AB, UK*

ARTICLE INFO

Keywords:
CO_2 capture
Electrospun nanofibers
Hydrodynamic cavitation
PEG
PMMA
CO_2-philicity

ABSTRACT

The increase in carbon dioxide (CO_2) emissions in recent years highlights the urgent need for advanced and effective CO_2 capture and release technologies. This study presents a two-step system aimed at first capturing CO_2 in water and subsequently releasing it using cavitation processes. Using multiple layers of horizontally oriented hydrophilic electrospun nanofibers sandwiched between layers of CO_2-philic nanofibers, we demonstrate a straightforward, reliable, efficient, and effective approach for dissolving pressurized CO_2-containing gas in water, followed by controlled release through cavitation mechanisms. These nanofibers are electrospun using poly(methyl methacrylate) (PMMA) and polyethylene glycol (PEG) polymers, and their physical and chemical properties and CO_2 absorption performance are characterized using thermogravimetric analysis, Fourier transform infrared spectroscopy (FTIR), differential scanning calorimetry (DSC), scanning electron microscopy (SEM), Brunauer–Emmett–Teller (BET) surface area analysis, and water contact angle measurements. The concentration, CO_2 absorption in water, cavitation-induced release, and the dynamic effect of bubbles were investigated by an in-situ adsorption setup. The nanofiber adsorbent was reported to have a specific surface area of 183 $m^2\ g^{-1}$ and a carbon adsorption capacity of 4 $mmol\ g^{-1}$. The cavitation process significantly enhanced CO_2 release efficiency, with bubble size changes strongly correlated with both adsorption and desorption rates. The CO_2-philic nanofibers effectively trap and release CO_2 molecules underwater, demonstrating enhanced dissolution and controlled release performance. This two-step capture-release system offers promising potential for applications in wastewater treatment, where controlled CO_2 release can be utilized for micropollutant removal, presenting a sustainable approach for both carbon management and water purification technologies.

1. Introduction

The rapid increase in atmospheric CO_2 concentration represents a critical global challenge, necessitating the urgent advancement of efficient carbon capture technologies. Over 2000 gigatons of CO_2 have been emitted by human activities since the Industrial Revolution, with emission rates continually rising [1]. To mitigate this, diverse carbon capture and storage (CCS) techniques, including direct air capture (DAC), membranes, multiphase absorption, adsorption, chemical looping combustion, calcium looping, and cryogenic methods, have been developed [2].

Among CCS approaches, DAC using hydroxide-based aqueous solutions is promising, yet its effectiveness is significantly limited by high regeneration energy demands (T > 800°C), often sourced from fossil fuel combustion which itself generates CO_2 emissions [3, 4, 5]. Another notable approach involves chemisorption of CO_2 onto porous materials functionalized with amine groups [6, 7]. Despite lower regeneration temperatures (80-120°C), this method faces constraints due to sorbent degradation, prompting ongoing research aimed at reducing energy consumption during regeneration [8, 9, 10].

Several emerging materials and methods, such as ionic membranes and zeolites, are being developed for carbon capture, but they remain predominantly at laboratory scale due to sorbent degradation and high operational costs [11, 12, 13, 14]. Alternative approaches utilizing porous solid adsorbents—including zeolites [15], porous carbons [16], porous organic polymers (POPs) [17], and metal-organic frameworks (MOFs) [18]—have gained significant attention in recent research.

Polyethylene glycol (PEG) demonstrates high potential for physical adsorption of CO_2 due to quadrupole-dipole interactions between CO_2 molecules and polar ether oxygen groups. The oxygen atom in CO_2 carries a partial negative charge due to its higher electronegativity, while the carbon atoms become slightly positively charged. CO_2-philic materials containing heteroatoms like oxygen, nitrogen, or fluorine serve as centers of negative charge that physically adsorb the positively charged carbon atoms in CO_2 molecules [19], resulting in significant selectivity over smaller gas molecules like N_2 [20]. Although PEG is inexpensive and environmentally benign, it is water-soluble, and low molecular weight PEG polymers exist in liquid form at

*Corresponding author. Email: fccebeci@sabanciuniv.edu
ORCID(s): 0000-0002-3118-0038 (F. Cebeci)

room temperature and atmospheric pressure [21], limiting their utility in aqueous media [22, 23, 24]. Consequently, blending or copolymerizing PEG in an insoluble polymer matrix emerges as an effective strategy for creating a water-stable, CO_2-philic material [25].

Poly(methyl methacrylate) (PMMA) exhibits hydrophobicity and water insolubility, rendering it a suitable polymer matrix for PEG incorporation. Systematic adjustment of PMMA-PEG ratios enables preparation of water-insoluble polymers with controlled hydrophilicity and CO_2-philicity parameters, potentially affecting the adsorption capacity and kinetics. While hydrophobicity modulation in polymeric materials under external pressure has been investigated, the specific CO_2-philicity behavior of PMMA-PEG blend systems under variable hydrodynamic conditions remains insufficiently characterized and need to be further studied [26, 27, 28]. Electrospinning produces high surface area nanofibrous membranes with controllable morphological and chemical properties. Electrospun fibers comprising PMMA-PEG blends exhibit properties conducive to CO_2 adsorption due to their high specific surface area and accessible functional groups. These CO_2-philic nanofibers can theoretically extend the interfacial contact time of CO_2 bubbles in solution, potentially enhancing mass transfer rates from the gas phase to the aqueous phase [10].

Silica nanoparticles have emerged as promising candidates for CO_2 capture applications due to their high specific surface area, tunable pore structure, and amenability to amine functionalization. Incorporating silica nanoparticles into the PMMA-PEG framework supplies a rigid, water-stable scaffold that suppresses PEG leaching, preserves membrane integrity, and adds an additional hierarchy of meso-/macroporosity. Their abundant surface silanol groups also offer in situ anchoring sites for PEG chains and subsequent amine grafting, creating a cooperative adsorption domain that amplifies CO_2 uptake while maintaining mechanical robustness in aqueous environments. Recent research has focused on investigating various morphologies and surface modifications to enhance CO_2 adsorption capacity, selectivity, and stability under diverse operating conditions. Eduardo et al. demonstrated the potential of amino-functionalized microporous silica nanoparticles modified with (3-aminopropyl)triethoxysilane (APTES), which exhibited enhanced CO_2 adsorption performance across both low and high pressure regimes, presenting a viable approach for CO_2 sequestration applications [29].

Hydrodynamic cavitation (HC) is characterized by rapid pressure fluctuations in fluid systems that induce phase transitions. Studies demonstrate that abrupt pressure decreases during hydrodynamic cavitation cause liquid evaporation, resulting in extensive bubble formation [30, 31, 26]. Pressure reduction facilitates the liberation of dissolved gases from the liquid phase in microfluidic devices, contributing to cavitation bubble nucleation and growth [32]. The rapid pressure gradients and introduction of nucleation sites via hydrodynamic cavitation accelerate CO_2 desorption from aqueous media [33], potentially offering kinetic advantages over conventional gas-liquid separation processes.

The combined application of electrospun CO_2-philic nanofibers with hydrodynamic cavitation presents a potential mechanism for enhancing carbon capture and release efficiency. When CO_2-philic porous materials are submerged in water while CO_2-containing gas passes through them, the bubble residence time in solution increases, which improves interfacial mass transfer. The electrospun nanofibers function as coalescence sites for nano and microbubbles suspended in the aqueous phase, facilitating the aggregation and extraction of CO_2 bubbles and thereby improving both absorption and desorption capacity in subsequent cycles [34]. Quantitative assessment of this combined approach is necessary to determine its efficacy for carbon capture and release from dilute CO_2 sources and to establish its thermodynamic and kinetic advantages over conventional methods. In this study, we developed a multilayer system of horizontally aligned electrospun nanofibers with alternating hydrophilic and CO_2-philic properties, fabricated from PMMA-PEG polymer blends with optimized ratios. We comprehensively characterized the physical, chemical, and mechanical properties of these nanofibers and quantified their CO_2 adsorption and cavitation-induced release performance. This two-step approach enables efficient CO_2 capture and controlled release from dilute sources through precise control of interfacial phenomena, offering potential applications in wastewater treatment where controlled CO_2 release can be utilized for micropollutant removal. This addresses a critical challenge in carbon management technology while maintaining operational simplicity and mechanical durability.

2. Materials and Methods

Polymethyl methacrylate (PMMA, $M_w = 200,000$ g/mol), Poly ethylene glycol(PEG) (average $M_n \sim 2000$), N,N-Dimethylformamide ($\geq 99\%$), Tetraethyl Orthosilicate (TEOS), Ammonia hydroxide solution 25%, and 2-Propanol (IPA, 99.5%) were purchased from Sigma Aldrich.

2.1. Solution preparation and electrospinning proccess

A mixture of PMMA/PEG dissolved in DMF was prepared as follows: Solutions were first prepared with polymer/solvent ratios of 10, 12, and 14 % (w/w). An electrospinning setup was assembled by attaching a plastic syringe to a metal needle with an internal diameter of 1 mm. Electrospinning was performed at accelerating voltages of 14 kV, 16 kV, and 20 kV. The stainless-steel collector had dimensions of 10 cm × 10 cm (100 cm^2), and the distance between the needle tip and the collector was set to 10 cm, 15 cm, or 20 cm. Flow rates were varied from 0.3 mL h^{-1} to 0.9 mL h^{-1}.

To select the most suitable proportion of polymer and solution, we spun three types of polymer blends formed of PMMA 20 wt%, 25 wt% PEG, and 30 wt% PEG at a constant

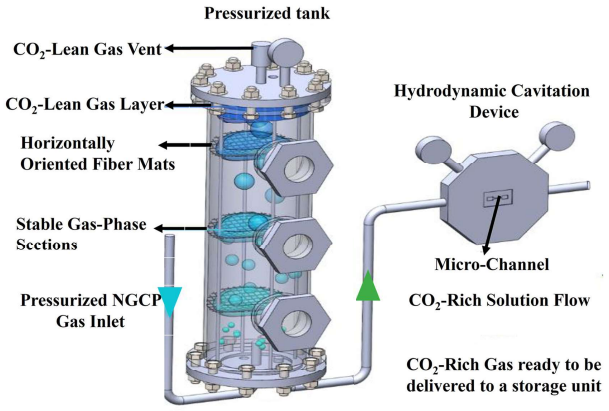


Figure 1: Experimental CO_2 capture setup.

polymer-solvent ratio of 12 wt%. Afterwards, we provided an analysis of these types. Moreover, we added silicate (SiO_2 or SiO_2H) nanoparticles (np) solutions, which were prepared according to the section below, into the electrospinning solution at a fixed solid-to-powder ratio: 6.5 wt% and polymer-to-powder ratio of 20:80.

During electrospinning, the overall process took place under conditions of room temperature and a relative humidity of 50%. Prior to electrospinning, the prepared solutions were constantly stirred for a period of one night at 45°C.

2.2. Synthesis of silica nanoparticles

We synthesized silica nanoparticles through a modified Stöber method [35]. Following literature and earlier research tetraethyl orthosilicate (TEOS) was added to an alcoholic solution as the precursor in reaction with water. The hydrolyzed precursors lost the EtOH group on them and joined together to form bigger molecules and finally they formed the silica nanoparticles. Introduction of ammonia into the solution lowers particles random directional growth which results in production of spherical particles [36].

2.3. Exprimental setup

The experimental CO_2 capture setup was established in three main stages; the pressurized tank, the HC microfluidic device, and the separation tank as shown in Fig. 1.

In the pressurized tank, the horizontally oriented hydrophilic and CO_2-philic nanofiber mats will provide stable CO_2-rich gas sections in the water column. Several layers of electrospun nanofiber filters are placed horizontally, vertically, and diagonally in the pressurized tank's filtration system. They ensure the bubbles are in a water medium to improve the dissolution process of CO_2. CO_2-philic nanofibers enhance the trapped gas process, whereas hydrophilic nanofiber filters will promote an augmented interface area for liquid gas at first, CO_2 is introduced in deionized water in such a way that the container is full. The pressurized tank has transparent sight glass windows which can withstand high levels of pressure to 100 bar . This setup allows for real-time bubble observation, METAGLAS® threaded sight glass windows being used together with Phantom VEO 710 high-speed cameras. Additionally, it indicates the user can observe the amount of air that dissolves in the bubbles and how they move abroad throughout the liquid. All reactor experimental tests were conducted in a clean room using highly stringent procedures associated with chip manufacturing standards to maintain flow patterns up to 150 psi. One microchannel with considerable upstream pressure is presented in our experimental setup. Current microfabrication techniques are used to create this device [37] . In this case, silicon and glass wafers will undergo an identical series of microfabrication techniques like wet etching, anodic bonding, photolithography, reactive ion etching (RIE), and plasma-enhanced chemical vapor deposition (PVCVD) by the preliminary process flow given.

Cavitating flows were generated at different upstream pressures and CO_2 concentrations (0.3 mg L^{-1} and 2 mg L^{-1}) at a fixed temperature of 23 °C in a microstep HC reactor with a 75 µm hydraulic diameter, designed and fabricated via standard microfabrication methods. Upstream pressure was applied by a pressurised nitrogen tank (Linde Gas, Gebze, Turkey) to push the CO_2 solution into the microscale HC reactor, and was monitored by means of a pressure gauge (Omega, Manchester, UK; 0.25 % FS accuracy, 0–3000 psi range). The microscale HC reactor comprises an inlet port, a short microchannel, and an outlet port. A custom sandwich holder firmly secures the chip to maintain a leak-free system. Key dimensions are listed in Table 1), and the fabrication workflow is illustrated in Fig. 2. First, a 2 µm ECI 3007 photoresist defined the channels and inlet/outlet ports on a 525 µm-thick silicon wafer (Fig. 2b). A 500 nm silicon-dioxide layer was then etched using an Advanced Plasma System (Fig. 2c). To relieve stress, 10 nm of titanium and 1 µm of aluminium were deposited on the wafer's backside with a DP650 magnetron sputter (Fig. 2d). Next, the port regions were selectively etched to a depth of 475 µm with AZ 10XT-60 resist in an SPTS Rapier etcher (Figs. 2e–f). The full pattern, including ports and channels, was subsequently etched 60 µm deep using the same resist and equipment (Fig. 2g). After etching, the aluminium, titanium, and SiO_2 layers were stripped via wet chemical processes (Figs. 2h–i). The wafer was cleaned in Piranha solution, then anodically bonded to a glass cover using an SB6 bonder (Fig. 2j). Further fabrication specifics are available in our previous work.

2.4. Observations and Optimization

Visualization was performed using a high-speed camera (Phantom VEO-710) equipped with a double-shutter CMOS sensor and a 4× lens. A cold-light halogen source (SOIF 5100-L) was used to illuminate the region of interest during recording. To enhance the clarity and contrast of images, image processing was performed with PCC software developed by Vision Research Inc. The high-speed imaging provided insights into the CO_2 dissolution rate and process efficiency by presenting bubble dynamics and, specifically, changes in volume and motion within the system. The bubble behaviour and motion were compared for cases without any

Table 1
Dimensions of the microscale HC reactor.

Extension Regions		Depth of Channel	Width of Channel	Length of Channel
Length (μm)	**Width** (μm)	(μm)	(μm)	(μm)
3962.5	900	60	100	75

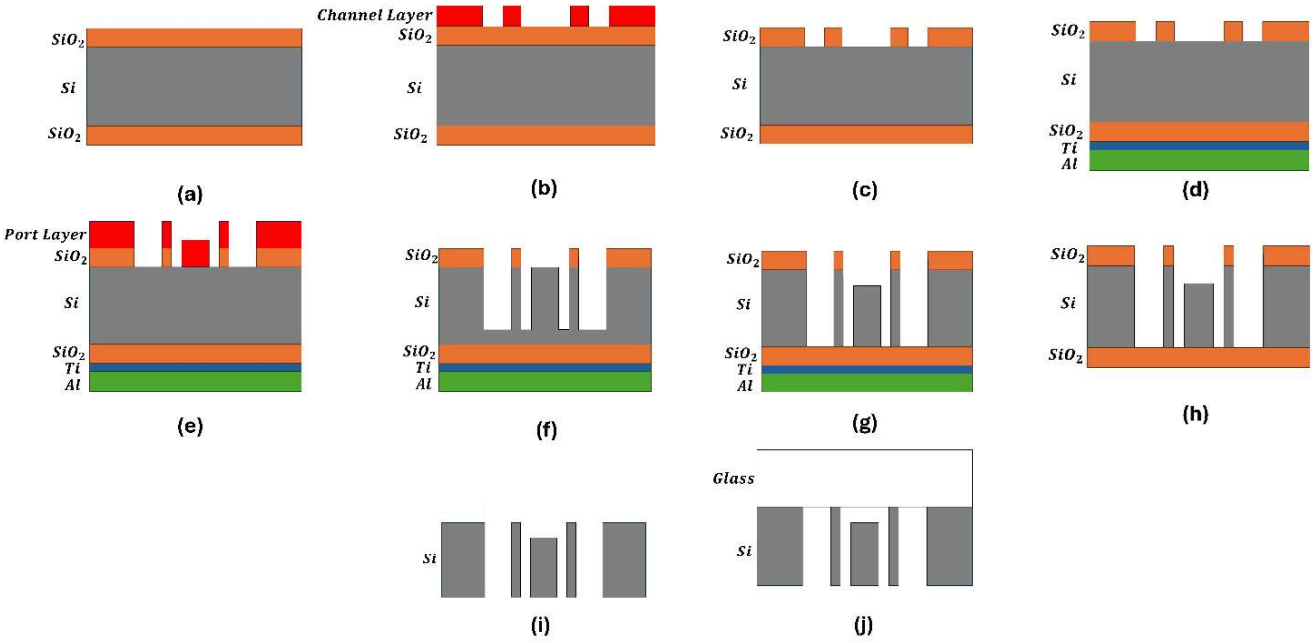


Figure 2: Microfabrication process steps. (a) SiO_2 deposition. (b) Patterning channels and ports by lithography. (c) Dry etching. (d) Sputtering of Ti and Al. (e) Patterning port layers. (f) Deep etching of ports. (g) DRIE of the entire pattern. (h) Wet etch of Al and Ti. (i) Wet etch of the SiO_2 mask. (j) Anodic bonding to glass.

obstacle, with a mesh that holds the nanofibres, and with the fabricated nanofibre inside the mesh. Analysis of the temporal evolution of bubble size, shape, and dissolution helps determine the rate of CO_2 dissolution into the water medium. This information is essential for optimising system parameters—such as gas-flow rate and nanofibre characteristics—to maximise dissolution efficiency. To calculate the average bubble diameter, bubble areas were measured in ImageJ and converted to diameters of equivalent circular bubbles; the mean diameter for each interval was then obtained. To calculate average bubble velocity, the displacement of each bubble tip during its ascension from bottom to top was tracked over seven cycles, and the mean value was reported. Images from the pressurised tank were acquired at 1000 frames per second (fps) with an exposure time of 200 μs and a resolution of 1280×800 pixels. For the microfluidic device, higher frame rates of 7500 fps and an exposure time of 133 μs were used because of the higher velocities in the restrictive channel.

3. Characterization

The morphologies of the nanofibers were characterized by using Scanning Electron Microscopy (SEM) (Jeol JSM 6010 LV and Supra 35VP Leo, Germany) to study the structural features and surface morphology of electrospun nanofibers relating to fiber arrangement and diameter, and it was revealed that the fibrous nature of the materials. The surface coverage, fiber diameter, and size distribution of fibrous materials were determined using the ImageJ software (National Institutes of Health, MD, USA). Fourier transformed-IR spectroscopy analysis (FTIR) analysis was used on the electrospun nanofibers for their molecular composition in details that gives information on specific functional groups present via a Thermo Scientific iS10 FTIR spectroscopy device. Thermogravimetric analysis is an effective method used in studying the thermal stability and decomposition properties of materials. In the light of electrospun nanofiber materials made of PMMA and PEG, it should be noted that Thermogravimetric Analysis (TGA) analysis provides useful information concerning weight alterations as well as thermal behavior displayed by such fibers via a Netzsch TGA-DTA device. Differential Scanning Calorimetry (DSC) analysis is a power technique that provides us with an insight into the thermal properties which are associated with different materials and show how they undergo changes in their state during heating or cooling. The main purpose of this work was to probe into thermal behavior as well as melting features of electrospun nanofibers via a Netzsch DSC

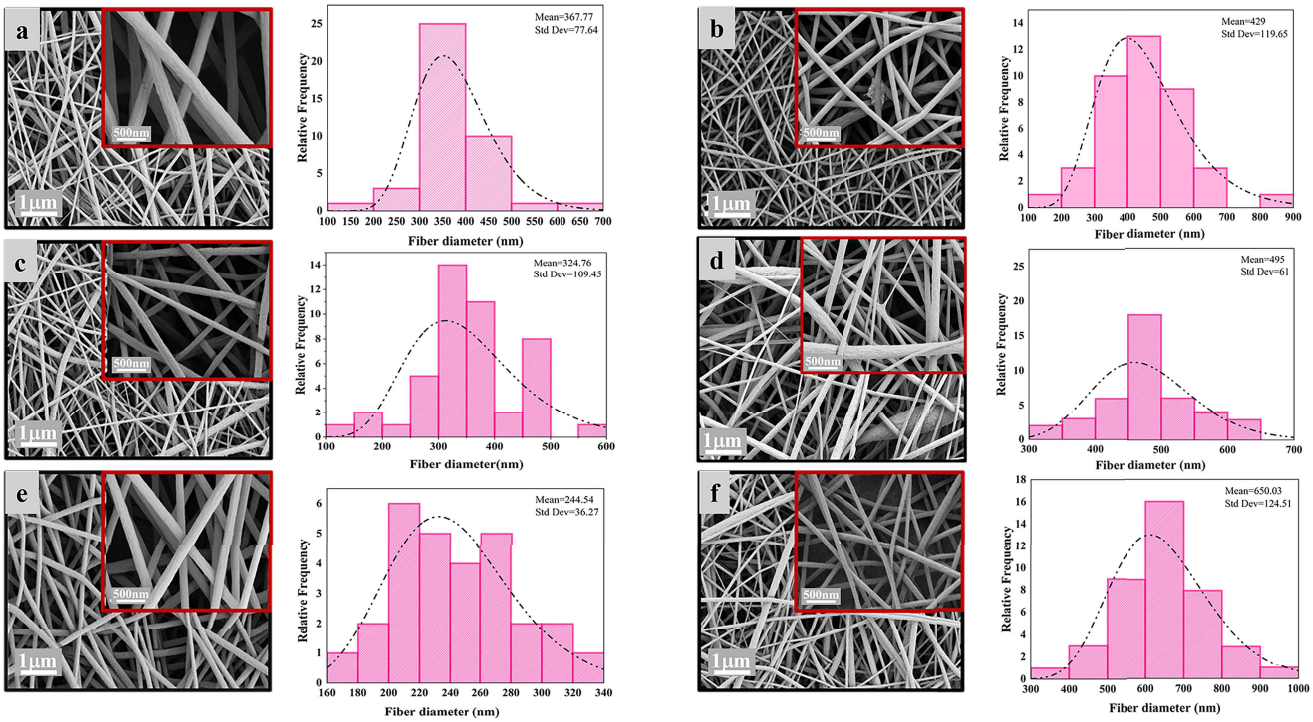


Figure 3: SEM images of PMMA-PEG a) 10 wt%, V = 16 kV, F.R.=0.6 mL h^{-1}, and D = 15 cm, b) 14 wt%, V = 14 kV, F.R.=0.3 mL h^{-1}, and D = 10 cm, c) 12 wt%, V = 14 kV, F.R.=0.3 mL h^{-1}, and D = 10 cm, d) 14wt%, V = 20kV, F.R.=0.6 mL h^{-1}, and D = 20 cm, e) 12 wt%, V = 20 kV, F.R.=0.6 mL h^{-1}, and D = 20 cm, f) 14wt%, V = 20kV, F.R.=0.9 mL h^{-1}, and D =20 cm .

device. The Brunauer–Emmett–Teller (BET) surface area and the porosity of the samples were studied by a nitrogen adsorption instrument. All the samples measured were degassed at 90 °C for 24 hr prior to actual measurements. Pore size distribution (PSD) and specific desorption pore volumes were obtained using the Barrett–Joy ner–Halenda (BJH) method, and desorption branches were used to determine the PSD via Micromeritics 3Flex device. Measurements of contact angles were conducted using the Attension Theta Lite. Distilled water was used as the wetting liquid. Droplet size was kept constant, and several measurements were taken for each sample ensuring accurate results were obtained. The contact angle values for the three specimens were analyzed and contrasted. Water contact angle is a significant parameter for assessing wettability and surface characteristics of substances [38].

4. Results and Discussion

4.1. SEM analysis

The flow rate at which a polymer solution comes out of the nozzle determines whether or not it will form beads as well as dictates the final fiber morphology. Increases in flow rates yielded larger fibers in all cases. Thus, maintaining a fine balance between solution feed rates and material escaping from the tip became a precondition for producing continuous fibers with minimal diameter [39].

Changing the distance between the needle and the collector will help in making sure that enough solvent evaporates before it can reach the collector, hence preventing the formation of beads. Longer distances made thinner threads which emphasized the significance of controlling this parameter carefully. Based on these observations, the electrospinning conditions were optimised to produce fibres with an average diameter of 244 nm from a 12 wt% (Fig. 3; Table 2); the operating window is an electric field of 20 kV, a flow rate of 0.6 mL h^{-1}, and a tip-to-collector distance of 20 cm.

4.1.1. Water contact angle measurement

Water contact angle measurements were conducted to study what effect the quantity of PEG had on how well PMMA-PEG electrospun nanofibers wettability. Two samples, one composed of PMMA and PEG in different combosition were made. In other words, we have PMMA-PEG 20% which has been classified as hydrophobic while PMMA-PEG30% has been termed as hydrophilic material.

The PMMA-PEG 20% sample showed an elevated contact angle because PMMA is inherently hydrophobic, a property that makes it water resistant. On the other hand, the PMMA-PEG 30% sample indicated a decreased contact angle since PEG is a hydrophilic polymer that attracts water molecules. The more PEG content found in this sample, thus heightening its hydrophilicity, causes reduction of contact angles. Results were obtained at different time intervals (0, 5, and 10 sec). It exhibited the highest contact angle, measuring 115°, among all the samples due to its hydrophobic nature of PMMA. Depending on PEG concentration, this

Table 2
Experimental Parameters and Sample Information of SEM Analysis

Concentration (wt%)	Flow Rate ($mL\,h^{-1}$)	Voltage (kV)	Distance (cm)
10	0.3	14	10
12	0.3	14	10
14	0.3	14	10
10	0.6	16	15
12	0.6	20	20
14	0.9	20	20

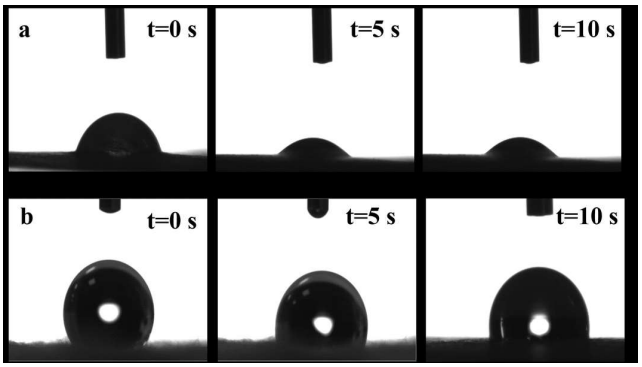


Figure 4: Contact angle for a) PMMA-30 wt% PEG and PMMA-20 wt% PEG at 0, 5 and 10 s .

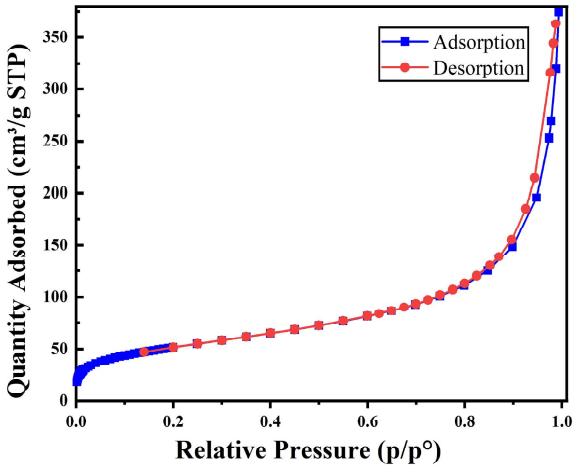


Figure 5: BET surface area analysis results: N_2-adsorption-desorption isotherm plots of PMMA-PEG-SiO_2 NPs.

droplet behavior diffuses into fibrous materials is shown in Fig. 4. The water-contact angle at $t = 0$ s decreased, indicating improved wettability as a result of increasing the PEG content to 30 wt %. This is evident from the significant decrease in the water contact angle at t = 0 s occasioned by the presence of PEG up to 30 wt%. A possible reason is that hydrophilic PEG molecules cause more adsorption and consequent spreading of water on different parts of the nanofiber structure. This happens because of coherent hydrogen bonds which exist between PEG and H_2 helping them blend well together and moisten fiber wall inches.

4.2. BET analysis

A nitrogen adsorption device was used to examine the samples' porosity and BET surface area. Before the measurements, all of the samples were degassed for 24 hr 90 °C. Pore size distribution (PSD) and specific desorption pore volumes were obtained using the Barrett–Joyner–Halenda (BJH) method, and desorption branches were used to determine the PSD. The mesoporous structure of the SiO_2 nanoparticles was confirmed by nitrogen adsorption and desorption isotherms (Fig. 5). A typical type IV isotherm seen in Fig. 5 confirms the mesoporous structure of silica.

At decreased relative pressures, the amount adsorbed slowly increases, which implies the adsorption of first few layers of the adsorbate molecules toward the sample's surface. Together, as the relative pressure increases towards 1, the amount adsorbed shows a steeper rise, which could suggest the development of more adsorption layers. The plateau we see here is at monolayer coverage showing that there are now diminishing returns from further increasing proportionate pressure. In this scope, it is very vital to look at the adsorption isotherm analysis that provides important information on the adsorption capacity of the sample, surface features, and porosity. Examination of quantity adsorbed behavior concerning relative pressure is essential for determining CO_2 capture applicability or other adsorption-based uses. An extensive analysis of the adsorption behavior and surface properties of sample PMMA-PEG- SiO_2 NPs is provided by the reciprocal plot of quantity adsorbed, which is 1/ [Q (p°/p - 1)]. In other words, this plot provides a different view of the adsorption process by taking the reciprocal of the Quantity Adsorbed. p/p° denotes Relative Pressure (p/p°) division of the actual pressure (p) by saturation pressure (p°) whereas Q elaborates on the quantity of the adsorbate molecules adsorbed per unit mass of the sample. Various trends can be seen on the plot as regards the range of from 0 to 0.007352 for 1/ [Q (p°/p - 1)] and from 0 to 0.3 for the Relative Pressure (p/p°). The inverse quantity adsorbed increases gradually at low values of relative pressure i.e., when gases are just being absorbed onto surfaces since they increase with time because there will always be more available adsorbate molecules than sites where they can get attached. Adsorbate molecules adsorb to surfaces through a process called adsorption, and this quantitatively yields a

Table 3
Summary of BET analysis results. Pore Volume (PV).

Sample	BET Surface Area ($m^2\ g^{-1}$)	Adsorption PV ($cm^3\ g^{-1}$)	Desorption PV ($cm^3\ g^{-1}$)	BJH Adsorption PV ($cm^3\ g^{-1}$)	BJH Desorption PV ($cm^3\ g^{-1}$)
PMMA-PEG-SiO_2	183.67	0.3069	0.3557	0.5626	0.5625
PMMA-PEG 20%	1.7263	0.0041	0.0052	0.0126	0.0126
PMMA-PEG 30%	1.9884	0.0027	0.0060	0.0105	0.0104

particular amount known as coverage. It is upon the completion of the monolayer that further adsorption results in the formation of additional layers. When the first sample is considered, it contains PMMA-PEG- SiO_2 nanoparticles that have a much larger BET surface area of 183.6746 $m^2\ g^{-1}$ than the other two samples, resulting in much more surface area for adsorption and hence greater potential for adsorbing molecules on it. Despite having high potential for adsorbing molecules, the surface area of the third sample is relatively low which results in less impact during adsorption compared to other sample (BJH adsorption and desorption). Based on these results, the first sample displays a relatively finer pore structure, with relatively lower average pore diameters and widths, hence suggesting a more extensive pore network as well as higher overall porosity. The first sample shows a BET surface area of 1.7263 $m^2\ g^{-1}$ significantly higher than PMMA-PEG 20% in the second sample, showing that the former has a higher degree of adsorption due to its broad surface area Such lower pore volumes and wider average pore diameters in sample 1 as compared to sample 2 shows that it is less porous, hence fewer active absorption sites. The BET surface area of sample three, PMMA-PEG 30%, is 1.9884 $m^2\ g^{-1}$, which is only a little higher than sample two, but quite a lot less than sample one. Although this sample has lower pore volumes than sample one, its porosity exceeds that of sample two. In terms of the average pore width and diameter, the third sample falls somewhere between the first and second samples, indicating a medium-sized pore system.

4.3. FTIR analysis

FTIR spectroscopy was performed using a Thermo Scientific iS10 device with a wavenumber range of 4000 cm^{-1}-400 cm^{-1}. The FTIR spectrum of PMMA is seen in Fig. 6 and it features distinct peaks that reveal the composition of the molecule. Within the nanofibers, there is a notable peak at 2960 cm^{-1}, which suggests that the methyl (CH_3) C-H bonds are stretching. Additionally, there's another relevant peak situated at 1732 cm^{-1}, which is indicative of an acrylate carboxyl groups; hence there exists ester linkages in PMMA [40]. In addition, there is a band at 1374 cm^{-1}, showing the bending vibrations of O-CH_3 groups, and the twisting mode of the CH_2 group in PMMA is reflected by a peak at 1239 cm^{-1}. Lastly, the presence of ester groups in the polymer chain, which is synthesized as PMMA, is affirmed by a notable peak at 1141 cm^{-1} [41]. In Fig. 6 FTIR Spectra of PEG had various distinct peaks. The band between 1100 $cm^{-1}$and 1300 cm^{-1} was caused by stretching

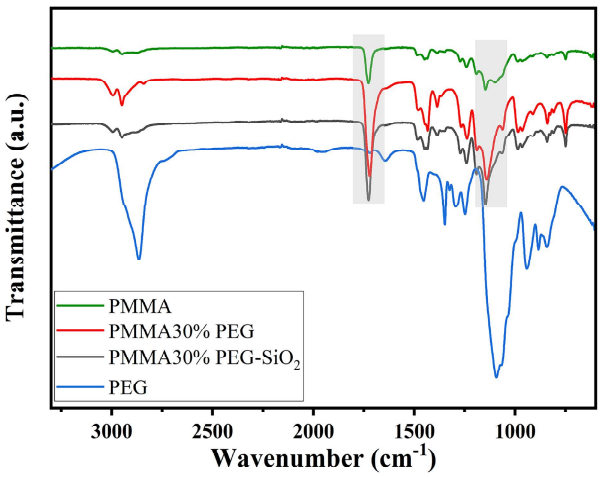


Figure 6: FTIR spectra of PMMA, PEG, and PMMA%30 PEG, and PMMA%30 PEG- SiO_2 NPs electrospun materials

vibrations of C-O ether groups' while them being in PEG framework; there were also alkyl (R-CH_2) stretching modes which could be easily seen at 2930 cm^{-1} confirming further incorporation into PEG, and hydroxyl (-OH) groups were detectable at 3489 cm^{-1} confirming that such groups are also present [42]. In addition, the FTIR analysis demonstrated that the silica nanoparticles had successfully been integrated within the electrospun nanofibers. Therefore, at around 689 $cm^{-1}$and 1100 cm^{-1}we detected characteristic peaks that can be attributed to the bending vibrations as well as asymmetric stretching oscillations for Si-O bonds contained in these silicon dioxide colloids. Furthermore, detectable is a zone which has a wavenumber of 3076 cm^{-1}, assigned to Si-OH stretching vibrations, signifying that hydroxyl groups are available on the surface of the silica nanoparticles. This observation indicated that water molecules find their way to the silica nanoparticles in the composite nanofiber, implying that it is water absorbing in effect, hence the hydrophilic nature is evident [43].

4.4. TGA analysis

Three samples were examined for percentage, according to the TGA results: PMMA-PEG (20%) for a hydrophobic sample, PMMA-PEG (30%) for a hydrophilic sample, and PMMA-PEG- SiO_2 for a CO_2-philic sample.

Analysis of the TGA data reveals that the hydrophobic and hydrophilic samples behaved similarly with small

Table 4
FTIR analysis of PMMA, PEG, their blends, and PMMA-PEG-SiO_2 composite.

PMMA		PEG		PMMA-20wt.%PEG		PMMA-30wt.%PEG		PMMA-30wt.%PEG-SiO_2	
Bond	Peak (cm^{-1})	Bond	Peak (cm^{-1})	Bond	Peak (cm^{-1})	Bond	Peak (cm^{-1})	Bond	Peak (cm^{-1})
C-H	2960	–OH	3489	C-H	2937	C-H	2949	–OH	3076
C=O	1732	C-H	2930	C=O	1743	C=O	1726	C-H	2949
C-O	1141	C-O-H	1100	O-C-O	1203	O-C-O	1147	C=O	1745
C-H	1446							C-H	1483
O-C-O	1710							O-Si-O	1105

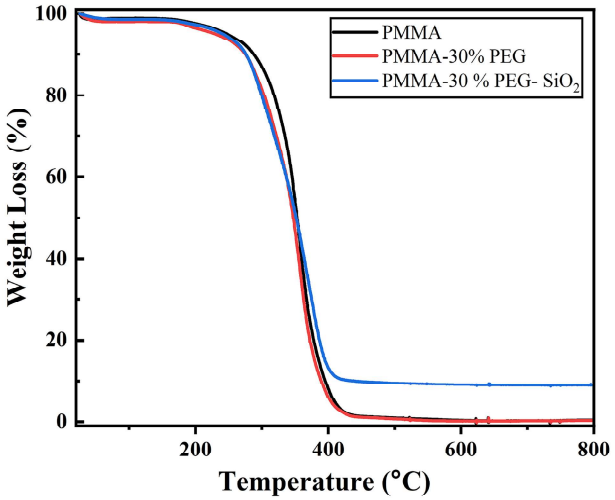


Figure 7: TGA diagram of a PMMA, PMMA-30 wt% PEG, and PMMA-30 wt% PEG- SiO_2 NPs electrospun materilas.

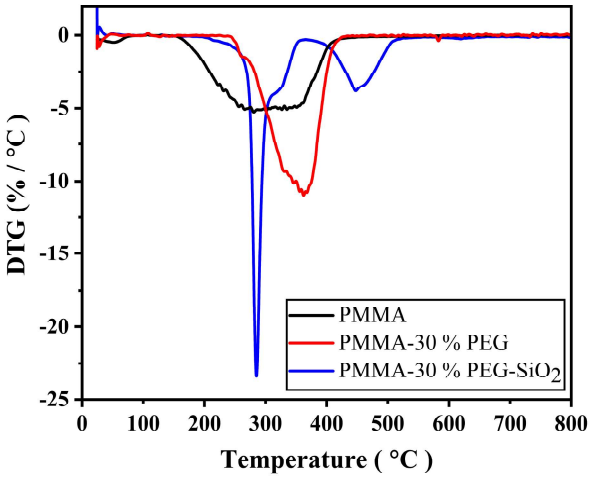


Figure 8: DTG diagram of a PMMA, PMMA-30 wt% PEG, and PMMA-30 wt% PEG- SiO_2 NPs electrospun materilas.

variations. However, there was a remarkable difference between the SiO_2-containing sample and other two indicating that SiO_2 content changed thermal properties of nanofiber composite. This is evidenced by the characteristic two-step weight loss pattern exhibited by both nanofibers during TGA analysis which implies that there are several degradation phases in operation under increasing temperature conditions. The PMMA-rich nanofiber showed more resistance to thermal decomposition by having higher remaining weight compared to other fiber type at elevated temperatures in relation to temperature stability. The first stage of weight had to do with breaking down of materials leading to the higher the temperature, the faster such reaction occurs and the more weight loss is observed in PEG and while the second stage was associated with the degradation of PMMA. The Fig. 7 TGA plots has been showing weight changes that all kinds of electrospun fibers had undergone with respect to different temperatures. Initially and at the beginning, there was little or minimal loss of mass at temperature below 100 °C due to desorption of water that had been adsorbed. This is only so because PMMA is made up hydrophobic molecules; this hinders it from taking up too much moisture hence making the loss insubstantial. Moving to the second stage, which happens at 250-300 °C, PMMA unsaturated chains decompose. Chain ends rupture causes loss of weight during this decomposition process. As for the third stage, a temperature above 300 °C means that polymer chains are degraded more leading to further loss of weight. The amount of weight lost at this point is affected by several things such as molecular weights in polymers besides other components like PEG. Additional mass loss steps are noticeable in the TGA graphs for electrospun PEG materials as shown in Fig. 7. At around 200 °C, the PEG breaks up ether bonds (CH_2OCH_2) thereby forming more stable methylene (CH_2) bonds which are produced through the process of thermal decomposition. This structural transformation leads to the release of small molecules thus causing weight decrease [44].

This is also a temperature range between 250 and 400 °C whereby PEG and PEG-composite fibers exhibit a degradation step in their TGA curves specific. A step as such accompanies the decomposition and evaporation of alcoholic compound mixtures. When the fiber is composed with PEG, the elecrospunn fibers bring in more pathways of decomposition along which weight loss exceeds that in similar fibers pure of PMMA alone. Silica nanoparticles will also make TGA examination look different. The presence of silica nanoparticles is confirmed by the distinct peaks that show up in the TGA curves. Peaks present at about 270 to 330 °C show up because there is silanol bonded water being released which shows that there are water molecules trapped inside these

Table 5
TGA analysis results

Sample	Temperature at Specified Weight Loss (°C)			
	5%	10%	50%	90%
PMMA	221.02	279.67	353.32	388.56
PMMA-20 wt% PEG	243.56	293.08	345.00	383.00
PMMA-30 wt% PEG	226.98	284.87	351.57	391.97
PMMA-30 wt% PEG-SiO_2 NPs	239.71	281.45	354.61	393.21

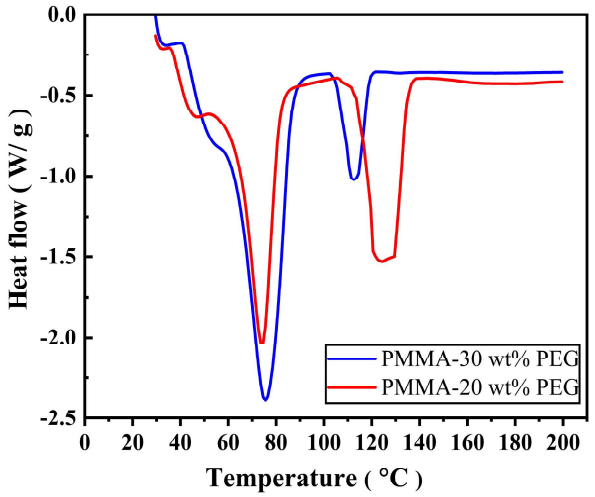


Figure 9: DSC Thermogram PMMA-20 wt% PEG and PMMA-30 wt% PEG.

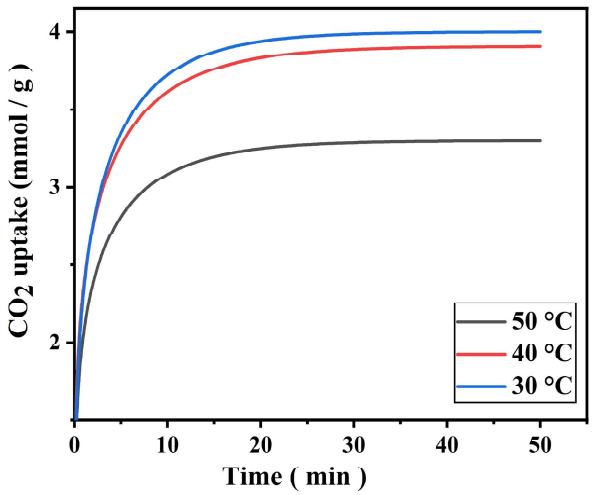


Figure 10: Adsorption capacity for PMMA-PEG- SiO_2 at different adsorption temperatures.

particles on absorption. Silanol bonded water takes more heat to remove as compared to other weight loss processes in TGA curves. When the temperatures surpass 500 °C, polymers decompose, leading to complete combustion of the polymer mass. However, the silica NPs embedded in the PMMA-30 wt% PEG- SiO_2/ NPs composite possess greater temperature stability. It is an evident fact showing that silica nanoparticles exist in the electrospun nanofibers withstanding heat effectively, thus an indication that they contribute to the total weight of these fibers.

4.5. DSC analysis

DSC is a powerful instrument that provides data on the amount of heat absorbed or emitted during physical processes such as melting and crystallization.

The purpose of the current work is to study the thermo-physical properties such as melting point of electrospun fine fibers from PMMA and PEG mixed at different ratios namely PMMA-PEG (20%) and PMMA-PEG (30%) which is shown in Fig. 9. During the heating scan, the DSC results showed a clearly defined endothermic peak, indicating that there was a clear thermal transition in the nanofiber. The position and intensity of the peak provide valuable information concerning the melting behavior of the material. This occurrence would be anticipated to take place at around PMMA's melting temperature, which falls between approximately 105 °C and 160 °C while PEG melts at around 70 °C. It was expected that the peak observed in the DSC graph would have a symmetrical appearance indicating that the melting was even. The magnitude of the peak represents the heat flow from phase transition to provide some information about how much energy is needed during that process. The presence of a distinct melting point in the DSC analysis of these electrospinning nanofibres signifies crystalline regions within them. A significant reduction in peak intensity is evident on increasing PEG content as shown by the DSC curve. Lower melting temperature is normally exhibited by PEG than in PMMA and therefore when large quantities are present it can delocalize crystallinity over all areas leading to weak peak signals. Moreover, a rise in PEG concentration makes the peak position shift to one at a lower temperature because PEG has a lower melting point compared to that of PMMA.

4.6. TGA analysis to evaluate the CO_2 -philicity of the nanofibers

To evaluate the stability and CO_2 uptake capabilities of the adsorbents we synthesized, TGA was used.

Every experiment required about 5 mg of adsorption material, which underwent conditioning at 100 degrees Celsius for 60 minutes inside an environment of nitrogen gas prior to testing the samples. This was implemented in order to remove any remaining moisture/other gases like CO_2 that might have been absorbed onto the surfaces of the samples.

The CO_2 capture steps were performed at temperatures of 30 °C, 40 °C, and 50 °C. (Fig. 10) In order to redo the samples, the temperature was raised to 120 °C at a rate of 10 °C min^{-1} until thorough reformation occurred. After the desorption phase, the chamber was again cooled to the adsorption temperature, and this was followed by a repetition of the whole process to resemble numerous adsorption/desorption rounds. In these tests, we used a low gas flow rate of 50 cm^3 min^{-1} so as to minimize the effect of external mass transfer onto the final findings [45]. The results show the level at which the CO_2 capture capacity (mmol of CO_2 captured per g of adsorbent, C_n, see Eq. 1) was attained.

$$C_n = \frac{(m_n - m_0)}{m_0} \times \frac{1000}{M_{CO_2}} \quad (1)$$

m_n: Mass of the sample at the end of the adsorption step in the nth cycle. m_0: the mass of the sample at the end of the desorption step at 120 °C (cycle n-1). M_{CO_2} is the molecular weight of CO_2 44 g mol^{-1}.

Our sample showed that when temperatures are low there is more absorption of carbon dioxide but is lower if temperatures get higher. This difference is due to various factors such as adsorption kinetic that at cold temperatures causes more carbon dioxide making this compound be captured better. The surface chemistry might also have a say in this, whereby, low temperatures escalate the interaction between the adsorbent and M_{CO_2} molecules. At such conditions the pore structure and distribution in the material will lead to better adsorption within it whereas the thermodynamics including change in the Gibbs free energy could be more favorable. Additional reactions at the material surface could be impacting the apparent tendency, in favor of M_{CO_2} adsorption over other reactions at lower temperatures.

4.7. Mechanical properties evaluation

A series of tensile tests were conducted to evaluate the mechanical properties of composite PEG electrospun nanofibers of PMMA. The stress-strain curves showing how samples behaved when they were loaded is shown in Fig. 11.

The chart indicates at which point each polymeric nanofiber failed as well as its final tensile stress and percent elongation at break. The mechanical properties of electrospun nanofibers can be significantly altered by the addition of nanoparticles. For example, mechanical testing has shown that incorporating silica nanoparticles into PMMA-30 wt% PEG resulted in a significant decrease in the ultimate tensile strength as compared to PMMA-20 wt% PEG and PMMA-30 wt% PEG. Consequently, there are several reasons for this reduced strength. Introducing nano particles to the nanofibers is one of the factors which can cause the misalignment of polymer chains and defects. Later, these defects can lead to failure and decrease in strength. Moreover, the distinction in stiffness among the polymer matrix and the silica nanoparticles could generate stress transfer inefficiencies which will lead to weaker interface bonding as well as sequential mechanical degradation. This calls for a regard on the trade-off between mechanical properties and other

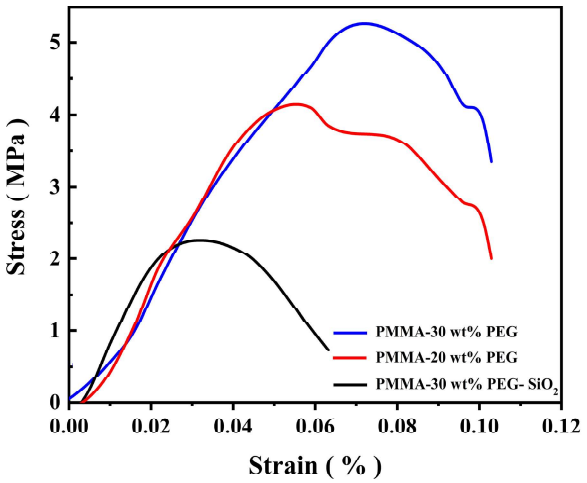


Figure 11: Stress-strain curves of three different samples of PMMA-20 wt% PEG, PMMA-30 wt% PEG and PMMA-30 wt% PEG- SiO_2 NPs

desirable properties that emerging nanoparticles may provide for better understanding. Even though the percentage of ultimate tensile strength might go down, they play a major role in enhancing functionalization and surface treatment capabilities of the nanofibers. Additionally, nano particles can affect the overall structure and orientation of nanofibres made by electrospinning [46]. Fiber alignment and diameter size can also be modified due to the presence of silica NPs thus affecting mechanical behavior. Consequently, in order for a given property like mechanical strength to be achieved it is important that the content of nanofillers is optimized carefully so that these are well distributed throughout the matrix.

4.8. Measurement of CO_2 Dissolution Rate in Water

A calibrated pH meter was used to measure the rate of dissolved CO_2 in water. In the beginning, the pH meter was calibrated using normal buffer solutions. To create a controlled environment, a tank was filled with deionized water. Thereafter, CO_2 gas was bubbled into the water after which the pH meter monitored the changes in pH over an extended period for the determination of CO_2 dissolution kinetics. The pH stabilization point was an indication of when the maximum capacity for CO_2 dissolution had been reached. At certain times, samples of water were taken to monitor the variations in pH. Such values were then employed in the development of a graphical illustration showing pH as a function of time; hence, an initial gradient could be determined as a measure of dissolution rate, which became apparent with steep gradients. The experiment was controlled in terms of temperature, pressure levels and concentrations of CO_2 for accurate analysis of dissolution kinetics under constant conditions.

4.9. Nanofibers and Liquid CO_2 Concentration

The effect of nanofibers on the concentration of CO_2 in the liquid phase in a pressure vessel is evaluated in this section. Within the pressurized tank is a complex netting unit consisting of several sheets of electrospun nanofiber filters oriented in different directions including horizontal placement while others are vertically or diagonally.Adsorption will be enhanced increasing CO_2 dissolution takes place in this pressurized tank through effective adsorbtion of CO_2 bubbles onto these fibers which also lock them up inside water containing medium thereby enabling maximum space possible for adsorbtion of gaseous carbon dioxide without any escape before time comes.The CO_2 philic nature of nanofibers help increase the CO_2/N_2 ratio in the trapped gas which increases efficiency of CO_2 dissolution. Furthermore, introduction of hydrophilic nanofibers would increase water penetration and provide high liquid-gas interface area hence promoting efficient mass transfer and consequently promoting CO_2 dissolution into water. During the first stage, tank is filled with deionized water and CO_2 gas was introduced to ensure that it was saturated then monitored by pH being constantly measured. Additionally, analyses of discrete water samples were taken at 0, 5, 10, 15, and 20 seconds to make observations on changes happening over time with respect to an increase or decrease in its dissolved CO_2 concentration levels by using phenolphthalein as an indicator during titration with sodium hydroxide solution (Fig. 12). At differential pressures samples are analyzed and thereby relieving gases which ensures accurate measurements by using vacuum chambers. It is calculated by multiplying the volume of titrated NaOH by 17.6 to determine the concentration of CO_2 in water samples. One mole of CO_2 reacts with two moles of NaOH. If the molar mass of CO_2 is 44 g mol^{-1} then, the amount of CO_2 neutralized by 1 mL of 0.02 mol L^{-1} NaOH is 0.88 mg. Hence, the conversion ratio between volume (millilitre) of NaOH and weight (milligram) of CO_2 per liter of a sample is 17.6. When the specified conditions are met, this method is essentially volumetric, so the concentration of dissolved CO_2 can be accurately determined. The reaction is described by Equation 2 [47]:

$$CO_2 + 2\,NaOH \longrightarrow Na_2CO_3 + H_2O \quad (2)$$

4.10. The dynamics of the rising bubbles in the pressurized tank

Dynamic investigations of bubble shapes and the effects of electrospun nanofibers are discussed in this section. Fig. 13 illustrates two cycles of the repetitive motion of bubbles within the flow in the absence of electrospun nanofibers. Firstly, the bubbles were recorded inside a container without the use of any mesh or nanofiber to understand the behavior of the bubbles during their motion. The average bubble diameter was measured as 13.9 mm, and the bubbles average flow speed was recorded as 0.374 m s^{-1} at an upstream pressure of 0.89 bar. Fig. 13 reveals that the bubble traverses the channel with slight changes in shape while maintaining a consistent size in the absence of electrospun nanofibers and the mesh leaving them as almost unchanged during their path except the amount that is being solved in the water.

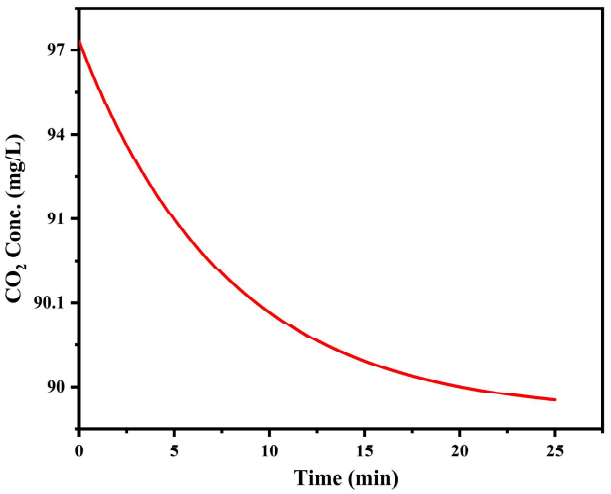


Figure 12: CO_2 Dynamics: Time-based variations in concentration.

Fig. 14 provides bubble motion through the holder and mesh, excluding electrospun nanofibers, at the same pressure. The bubbles consistently exit the mesh without undergoing significant alterations in their behavior in terms of size and velocity. The bubbles are observed to be retained behind the mesh until a specific amount of gas bubbles accumulate behind mesh. Beyond this threshold, they pass through the mesh without undergoing substantial changes in size and shape. The bubble speed was recorded to be 0.35 m s^{-1}, which is slightly lower than the case of no mesh. The speeds of bubble passage before mesh and after mesh are identical.

Fig. 15 provides images of bubble passage in the presence of nanofibers under the same conditions. The bubbles interacting with the electrospun nanofibers are observed to pass after being adsorbed by the nanofiber with much more delay (of 99µs). The bubble speed after complete separation from nanofiber is not different than the two previous cases, i.e. without mesh and with mesh only. However, the speed of the tip of the bubble that is formed during its passage through the nanofiber is increased to 0.47 m s^{-1}, which is due to substantial deformation of the bubble as well as its motion.

It is clear from Fig. 15 that the bubbles rise in their path towards the surface without interacting with each other. By analyzing the area covered by the bubble, it can be observed that the area of bubble exiting nanofiber (from 30 ms to 40 ms) increases from 120.78 mm^2 to 171.76 mm^2. One possible explanation for this phenomenon is linked to the adsorption of CO_2 onto the material's surface. CO_2 molecules are attracted to and trapped on the surface of the CO_2-philic nanofiber. Fig. 15 provides an illustrative schematic of this process. The size of the bubbles decreases as CO_2 is adsorbed because the gas molecules practically adhere to the nanofiber. CO_2 is extracted from the gas stream through

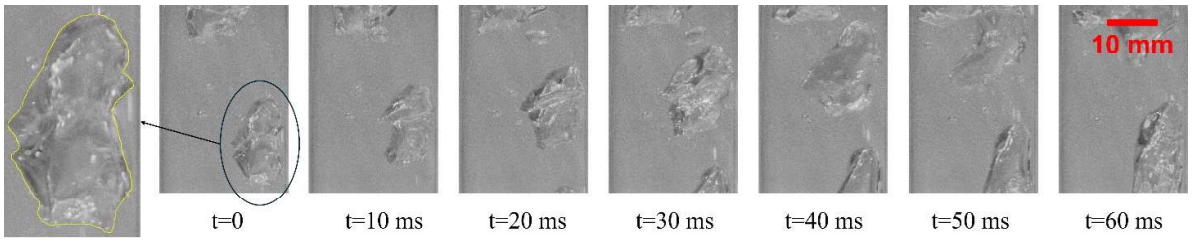


Figure 13: Time evolution of bubble behavior through the channel at an upstream pressure of 0.89 bar.

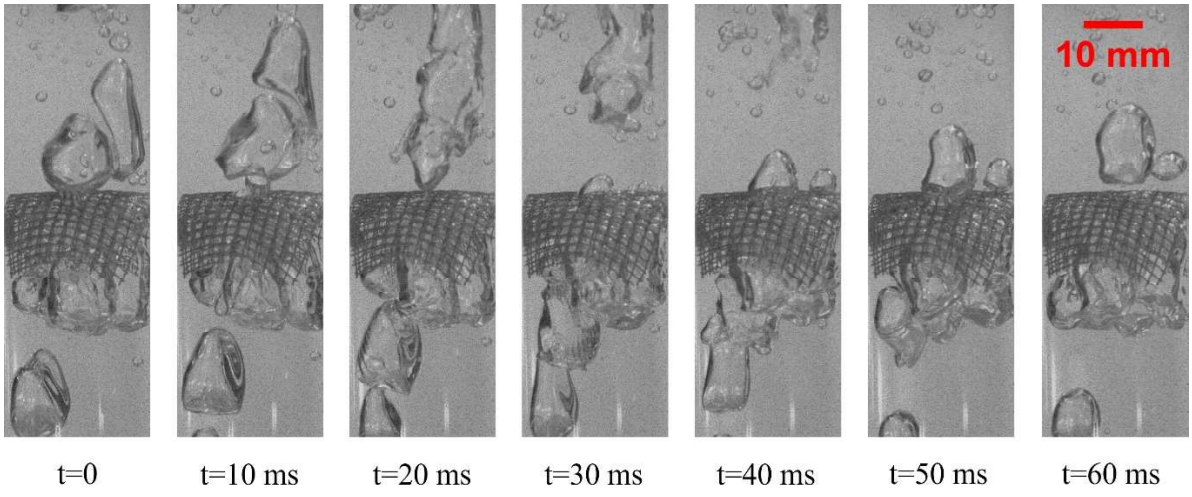


Figure 14: Time evolution of bubble behavior in the presence of mesh holder at an upstream pressure of 0.89 bar.

this process, which is an essential part of the separation and capture mechanism.

4.11. Cavitating flow patterns inside microscale HC reactor

As soon as the jet leaves the microchannel, its behavior depends strongly on the upstream pressure and dissolved CO_2 concentrations. At 0.69 MPa, only a thin streak of vapor forms along the lower edge as incipient shear cavitation (Fig. 16a) roughly a millimeter before it disappears again at low concentration. At a higher CO_2 concentration of $2\,\mathrm{mg\,L^{-1}}$, a developing cavity can be observed with separated bubbles, which can clearly be considered as isolated CO_2 bubbles (Fig. 16d). This is deduced from the observations at the much lower CO_2 concentration, where such bubbles are not even visible. The flow loops back on itself just behind this streak, and that gentle recirculation keeps the cavity toward the bottom (Fig. 16a).

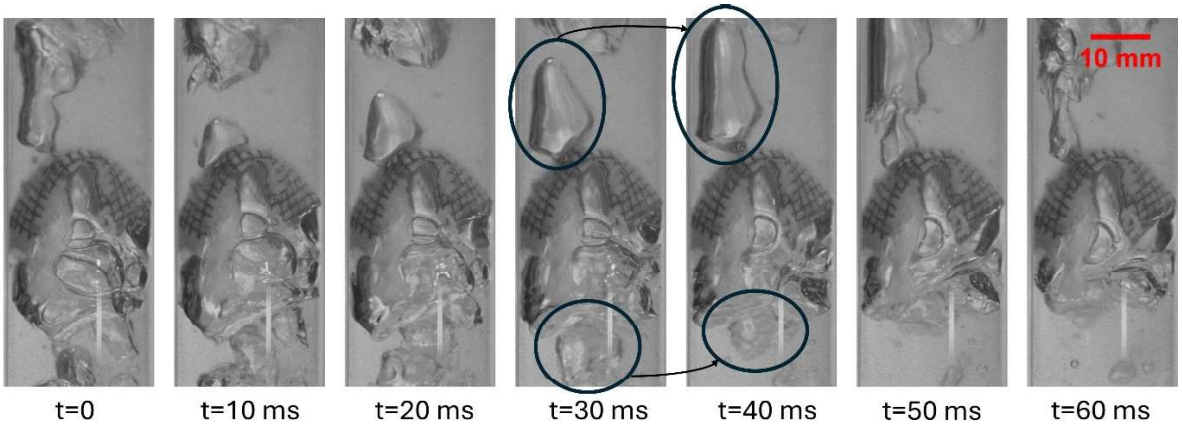


Figure 15: Time evolution of bubble behavior in the presence of nanofiber at an upstream pressure of 0.89 bar.

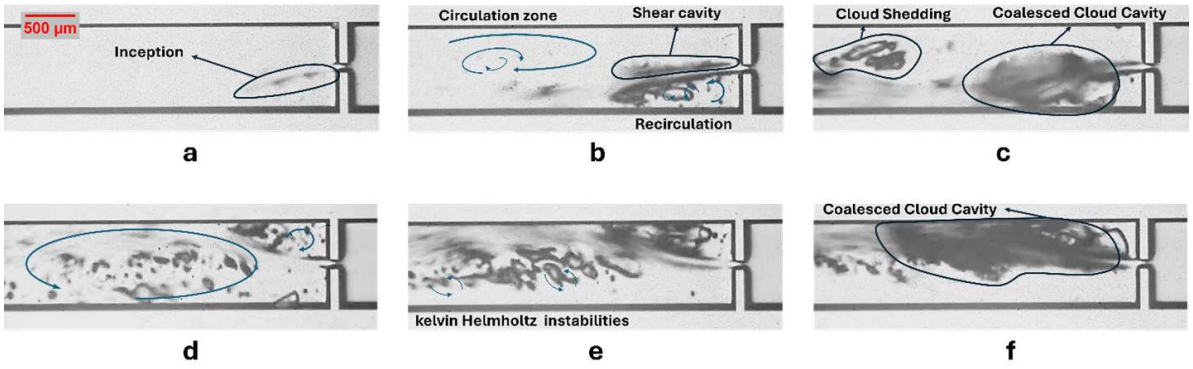


Figure 16: Cavitating flow patterns for a solution with low CO_2 concentration ($0.3\,mg\,L^{-1}$) at upstream pressures of (a) 0.69 MPa, (b) 1.38 MPa, and (c) 2.76 MPa, and for a solution with high CO_2 concentration ($2\,mg\,L^{-1}$) at upstream pressures of (d) 0.69 MPa, (e) 1.38 MPa, and (f) 2.76 MPa.

When the pressure increases to 1.38 MPa, at low concentration vapor appears on both the upper and lower edges. These two cavities grow side by side with a narrow liquid core between them. Every few hundred microseconds, the flow pinches off the tips of the cavities, so small cloud-like bubbles detach, drift a short distance, and collapse. A stronger circulation roll now fills the whole jet thickness and feeds liquid back toward the pinch-off point, sustaining this regular cycle (Fig. 16b). At higher concentration, more bubbles are formed in the circulation zone, and Kelvin–Helmholtz instabilities begin to appear.

At the highest upstream pressure of 2.76 MPa and low CO_2 concentration, the twin cavities widen after the jet exits the channel and quickly join, forming one broad vapor core that extends well beyond the outlet (Fig. 16c). The circulation roll grows longer and stronger, and cloud detachment becomes roughly 50% more rapid. In every case, a recirculation zone is present, but it expands and intensifies as the pressure rises. Thus, the flow evolves from a single inception cavity, to developing twin cavities with regular cloud breakup, and finally to a merged, fully cavitating core with an almost continuous cloud detachment. At higher CO_2 concentration, the coalesced cloud is much thicker and penetrates almost down to the end of the channel, forming a fully developed cavity. Kelvin–Helmholtz instabilities are also visible downstream.

5. Conclusion

This study developed and assessed a two-step carbon capture and release system based on electrospun PMMA-PEG nanofiber membranes combined with hydrodynamic cavitation. The use of nanofibers with both hydrophilic and CO_2-philic properties promoted the physical adsorption and dissolution of CO_2 into water, followed by controlled release through cavitation processes. Membranes produced with optimized polymer ratios and controlled electrospinning parameters achieved a specific surface area of $183\,m^2\,g^{-1}$ and a CO_2 adsorption capacity of $4\,mmol\,g^{-1}$. These characteristics demonstrate the impact of material composition and process control on the effectiveness of carbon capture and release membranes. The experimental results showed that hydrodynamic cavitation significantly enhanced both CO_2 dissolution and subsequent release by reducing bubble size and increasing mass transfer efficiency during both capture and desorption phases. This enhancement can be attributed to the interaction between the membrane surface and the dynamic conditions created by cavitation. The membrane maintained high performance even with low concentrations of CO_2, indicating its suitability for industrial applications. The methods employed—electrospinning and hydrodynamic cavitation—are straightforward to implement and can be scaled up, making this two-step approach practical for larger-scale carbon management processes. The reliability of the system was strengthened by the validation of the nanofibers' structural and functional characteristics through the combined use of advanced characterization techniques, including TGA, FTIR, DSC, SEM, BET, and water contact angle measurements. The findings provide valuable insights and demonstrate a viable technological pathway for addressing carbon management challenges through integrated capture-release systems. The approach described here supports the development of energy-efficient and scalable solutions for reducing atmospheric CO_2 and contributes to broader environmental sustainability goals.

6. Acknowledgments

The authors gratefully acknowledge the financial support provided by The Scientific and Technological Research Council of Turkey (TÜBİTAK) under project number 221M522.

References

[1] M. Osazuwa-Peters, M. Hurlbert, Analyzing regulatory framework for carbon capture and storage (ccs) technology development: A case study approach, The Central European Review of Economics and Management 4 (1) (2020) 107–148. doi:10.29015/cerem.834.

[2] M. Bui, C. S. Adjiman, A. Bardow, E. J. Anthony, A. Boston, S. Brown, P. S. Fennell, S. Fuss, A. Galindo, L. A. Hackett, J. P. Hallett, H. J. Herzog, G. Jackson, J. Kemper, S. Krevor, G. C. Maitland, M. Matuszewski, I. S. Metcalfe, C. Petit, G. Puxty, J. Reimer, D. M. Reiner, E. S. Rubin, S. A. Scott, N. Shah, B. Smit, J. P. M. Trusler, P. Webley, J. Wilcox, N. Mac Dowell, Carbon capture and storage (ccs): The way forward, Energy and Environmental Science 11 (5) (2018) 1062–1176. doi:10.1039/c7ee02342a.

[3] R. Baciocchi, G. Storti, M. Mazzotti, Process design and energy requirements for the capture of carbon dioxide from air, Chemical Engineering and Processing: Process Intensification 45 (12) (2006) 1047–1058. doi:10.1016/j.cep.2006.03.015.

[4] D. W. Keith, G. Holmes, D. St. Angelo, K. Heidel, A process for capturing co_2 from the atmosphere, Joule 2 (8) (2018) 1573–1594. doi:10.1016/j.joule.2018.05.006.

[5] M. Mazzotti, R. Baciocchi, M. J. Desmond, R. H. Socolow, Direct air capture of co_2 with chemicals: Optimization of a two-loop hydroxide carbonate system using a countercurrent air-liquid contactor, Climatic Change 118 (1) (2013) 119–135. doi:10.1007/s10584-012-0679-y.

[6] W. Andreoni, F. Pietrucci, Co_2 capture in amine solutions: Modelling and simulations with non-empirical methods, Journal of Physics: Condensed Matter 28 (50) (10 2016). doi:10.1088/0953-8984/28/50/503003.

[7] X. Wang, Effects of nanoparticles on the properties of cement-based materials (2018).
URL https://lib.dr.iastate.edu/etd/16236

[8] C. Gebald, J. A. Wurzbacher, P. Tingaut, T. Zimmermann, A. Steinfeld, Amine-based nanofibrillated cellulose as adsorbent for co_2 capture from air, Environmental Science & Technology 45 (20) (2011) 9101–9108. doi:10.1021/es202223p.

[9] A. Goeppert, M. Czaun, G. K. S. Prakash, G. A. Olah, Air as the renewable carbon source of the future: An overview of co_2 capture from the atmosphere, Energy & Environmental Science 5 (7) (2012) 7833–7853. doi:10.1039/c2ee21586a.

[10] H. A. Patel, S. H. Je, J. Park, D. P. Chen, Y. Jung, C. T. Yavuz, A. Coskun, Unprecedented high-temperature

co_2 selectivity in n_2-phobic nanoporous covalent organic polymers, Nature Communications 4 (2013). doi:10.1038/ncomms2359.

[11] K. S. Lackner, Capture of carbon dioxide from ambient air, European Physical Journal: Special Topics 176 (1) (2009) 93–106. doi:10.1140/epjst/e2009-01150-3.

[12] E. S. Sanz-Pérez, C. R. Murdock, S. A. Didas, C. W. Jones, Direct capture of co_2 from ambient air, Chemical Reviews 116 (19) (2016) 11840–11876. doi:10.1021/acs.chemrev.6b00173.

[13] J. V. Veselovskaya, V. S. Derevschikov, T. Y. Kardash, O. A. Stonkus, T. A. Trubitsina, A. G. Okunev, Direct co_2 capture from ambient air using k_2co_3/al_2o_3 composite sorbent, International Journal of Greenhouse Gas Control 17 (2013) 332–340. doi:10.1016/j.ijggc.2013.05.006.

[14] S. Ghobadi, L. I. Şanlı, R. Bakhtiari, S. A. Gürsel, Green composite papers via use of natural binders and graphene for PEM fuel cell electrodes, ACS Sustainable Chemistry & Engineering 5 (9) (2017) 8407–8415. doi:10.1021/acssuschemeng.7b02207.
URL https://doi.org/10.1021/acssuschemeng.7b02207

[15] H. Mashhadimoslem, M. A. Abdol, K. Zanganeh, A. Shafeen, A. A. AlHammadi, M. Kamkar, A. Elkamel, Development of the co_2 adsorption model on porous adsorbent materials using machine learning algorithms, ACS Applied Energy Materials 7 (19) (2024) 8596–8609. doi:10.1021/acsaem.4c01465.
URL https://doi.org/10.1021/acsaem.4c01465

[16] H. Mashhadimoslem, M. Vafaeinia, M. Safarzadeh, A. Ghaemi, F. Fathalian, A. Maleki, Development of predictive models for activated carbon synthesis from different biomass for co_2 adsorption using artificial neural networks, Industrial & Engineering Chemistry Research 60 (38) (2021) 13950–13966. doi:10.1021/acs.iecr.1c02754.
URL https://doi.org/10.1021/acs.iecr.1c02754

[17] P. Bhanja, A. Modak, A. Bhaumik, Porous organic polymers for co_2 storage and conversion reactions, ChemCatChem 11 (1) (2019) 244–257. arXiv:https://chemistry-europe.onlinelibrary.wiley.com/doi/pdf/10.1002/cctc.201801046, doi:10.1002/cctc.201801046.
URL https://chemistry-europe.onlinelibrary.wiley.com/doi/abs/10.1002/cctc.201801046

[18] H. Mashhadimoslem, M. A. Abdol, P. Karimi, K. Zanganeh, A. Shafeen, A. Elkamel, M. Kamkar, Computational and machine learning methods for co_2 capture using metal–organic frameworks, ACS Nano 18 (35) (2024) 23842–23875. doi:10.1021/acsnano.3c13001.
URL https://doi.org/10.1021/acsnano.3c13001

[19] H. Mashhadimoslem, M. Safarzadeh Khosrowshahi, M. Jafari, A. Ghaemi, A. Maleki, Adsorption equilibrium, thermodynamic, and kinetic study of $o_2/n_2/co_2$ on functionalized granular activated carbon, ACS Omega 7 (22) (2022) 18409–18426. doi:10.1021/acsomega.2c00673.
URL https://doi.org/10.1021/acsomega.2c00673

[20] O. Aschenbrenner, P. Styring, Comparative study of solvent properties for carbon dioxide absorption, Energy & Environmental Science 3 (8) (2010) 1106–1113. doi:10.1039/c002915g.

[21] S. Ghobadi, S. Mehraeen, R. Bakhtiari, B. Shamloo, V. Sadhu, M. Papila, F. Ç. Cebeci, S. A. Gürsel, PVA/PANI/rGO ternary electrospun mats as metal-free anti-bacterial substrates, RSC Advances 6 (9) (2016) 92434–92442. doi:10.1039/C6RA16785C.

[22] A. Car, C. Stropnik, W. Yave, K. V. Peinemann, Pebax®/polyethylene glycol blend thin film composite membranes for co_2 separation: Performance with mixed gases, Separation and Purification Technology 62 (1) (2008) 110–117. doi:10.1016/j.seppur.2008.01.001.

[23] P. Van Ginderen, W. A. Herrebout, B. J. Van der Veken, Van der waals complex of dimethyl ether with carbon dioxide, Journal of Physical Chemistry A 107 (28) (2003) 5391–5396. doi:10.1021/jp034553i.

[24] H. J. Kim, C. S. Kim, S. H. Yang, D. H. Lee, Fly ash incorporated polyurethane electrospun membrane for co_2 absorption, Digest Journal of Nanomaterials and Biostructures 10 (2) (2015) 595–601.

[25] Y. Gao, C. Yu, M. Chen, X. Wang, D. Zhou, G. Xue, Thermo-reversible gelation of atactic poly(methyl methacrylate) in poly(ethylene glycol) oligomers, European Physical Journal E 36 (4) (2013). doi:10.1140/epje/i2013-13037-8.

[26] A. S. Aghdam, F. R. Talabazar, M. Jafarpour, A. Koşar, F. Ç. Cebeci, M. Ghorbani, New nanofiber composition for multiscale bubble capture and separation, ACS Omega 7 (44) (2022) 39959–39969. doi:10.1021/acsomega.2c04426.

[27] M. Jafarpour, A. S. Aghdam, A. Koşar, F. Çakmak Cebeci, M. Ghorbani, Electrospinning of ternary composite of pmma-peg-sio2 nanoparticles: Comprehensive process optimization and electrospun properties, Materials Today Communications 29 (2021) 102865. doi:https://doi.org/10.1016/j.mtcomm.2021.102865.
URL https://www.sciencedirect.com/science/article/pii/S2352492821008539

[28] M. A. Samaha, H. V. Tafreshi, M. Gad-el Hak, Influence of flow on longevity of superhydrophobic coatings, Langmuir 28 (25) (2012). doi:10.1021/la301299e.

[29] E. J. Cueto-Díaz, F. Suárez-García, S. Gálvez-Martínez, M. P. Valles-González, E. Mateo-Marti, CO2 adsorption capacities of amine-functionalized microporous silica nanoparticles, Reactive and Functional Polymers 170 (Jan 2022). doi:10.1016/j.reactfunctpolym.2021.105100.

[30] P. R. Gogate, A. B. Pandit, A review and assessment of hydrodynamic cavitation as a technology for the future, Ultrasonics Sonochemistry 12 (1) (2005) 21–27. doi:10.1016/j.ultsonch.2004.03.007.
URL https://www.sciencedirect.com/science/article/pii/S1350417704001002

[31] Facile hydrodynamic cavitation on chip via cellulose nanofibers stabilized perfluorodroplets inside layer-by-layer assembled slips surfaces, Chemical Engineering Journal 382 (2020) 122809. doi:https://doi.org/10.1016/j.cej.2019.122809.
URL https://www.sciencedirect.com/science/article/pii/S1385894719322193

[32] M. Ghorbani, A. K. Sadaghiani, L. G. Villanueva, A. Koşar, Hydrodynamic cavitation in microfluidic devices with roughened surfaces, Journal of Micromechanics and Microengineering 28 (7) (2018) 075016. doi:10.1088/1361-6439/aab9d0.
URL https://doi.org/10.1088/1361-6439/aab9d0

[33] S. F. Jones, G. M. Evans, K. P. Galvin, Bubble nucleation from gas cavities – a review, Advances in Colloid and Interface Science 80 (1) (1999) 27–50. doi:10.1016/S0001-8686(98)00074-8.
URL https://www.sciencedirect.com/science/article/pii/S0001868698000748

[34] T. Zhao, Z. Liu, A novel analysis of carbon capture and storage (ccs) technology adoption: An evolutionary game model between stakeholders, Energy 189 (12 2019). doi:10.1016/j.energy.2019.116352.

[35] M. Barak, A. S. Aghdam, E. B. S. Ozbulut, S. Unal, F. Ç. Cebeci, Layer-by-layer assembly of nanofilms from colloidally stable amine-functionalized silica nanoparticles, Colloids and Surfaces A: Physicochemical and Engineering Aspects 630 (2021) 127615. doi:10.1016/j.colsurfa.2021.127615.
URL https://www.sciencedirect.com/science/article/pii/S0927775721014849

[36] J. Jafarpour, Electrospinning of ternary composite of pmma-peg-sio_2 nanoparticles: Comprehensive process optimization and electrospun properties, Materials Today Communications 29 (2021) 102865. doi:10.1016/j.mtcomm.2021.102865.
URL https://www.sciencedirect.com/science/article/pii/S2352492821008539

[37] A. S. Aghdam, M. Ghorbani, G. Deprem, F. Ç. Cebeci, A. Koşar, A new method for intense cavitation bubble generation on layer-by-layer assembled slips, Scientific Reports 9 (1) (2019) 11600. doi:10.1038/s41598-019-47954-y.
URL https://www.nature.com/articles/s41598-019-47954-y

[38] S. Krainer, U. Hirn, Contact angle measurement on porous substrates: Effect of liquid absorption and drop size, Colloids and Surfaces A: Physicochemical and Engineering Aspects 619 (2021) 126503. doi:10.1016/j.colsurfa.2021.126503.
URL https://www.sciencedirect.com/science/article/pii/S0927775721003721

[39] R. Stepanyan, A. V. Subbotin, L. Cuperus, P. Boonen, M. Dorschu, F. Oosterlinck, M. J. H. Bulters, Nanofiber diameter in electrospinning of polymer solutions: Model and experiment, Polymer 97 (2016) 428–439. doi:10.1016/j.polymer.2016.05.045.
URL https://www.sciencedirect.com/science/article/pii/S0032386116304359

[40] V. Parthasarathy, R. S. Nakandhrakumar, S. Mahalakshmi, P. S. Kumar, B. Sundaresan, Structural, optical, thermal and non-isothermal decomposition behavior of pmma nanocomposites, Journal of Inorganic and Organometallic Polymers and Materials 30 (8) (2020) 2998–3013. doi:10.1007/s10904-020-01558-2.
URL https://link.springer.com/article/10.1007/s10904-020-01558-2

[41] G. Soni, S. Srivastava, P. Soni, P. Kalotra, Y. K. Vijay, Optical, mechanical and structural properties of pmma/sio_2 nanocomposite thin films, Materials Research Express 5 (1) (2018) 015302. doi:10.1088/2053-1591/aaa0f7.
URL https://iopscience.iop.org/article/10.1088/2053-1591/aaa0f7

[42] H. S. Mansur, R. L. Oréfice, A. A. P. Mansur, Characterization of poly(vinyl alcohol)/poly(ethylene glycol) hydrogels and pva-derived hybrids by small-angle x-ray scattering and ftir spectroscopy, Polymer 45 (21) (2004) 7193–7202. doi:10.1016/j.polymer.2004.08.036.

[43] I. M. Joni, L. Nulhakim, M. Vanitha, C. Panatarani, Characteristics of crystalline silica (sio_2) particles prepared by simple solution method using sodium silicate (na_2sio_3) precursor, Journal of Physics: Conference Series 1080 (2018) 012006. doi:10.1088/1742-6596/1080/1/012006.
URL https://iopscience.iop.org/article/10.1088/1742-6596/1080/1/012006

[44] X. M. Hu, D. M. Wang, W. M. Cheng, G. Zhou, Effect of polyethylene glycol on the mechanical property, microstructure, thermal stability, and flame resistance

of phenol–urea–formaldehyde foams, Journal of Materials Science 49 (4) (2014) 1556–1565. doi:10.1007/s10853-013-7838-z.
URL https://doi.org/10.1007/s10853-013-7838-z

[45] M. Tahmasebpoor, M. Iranvandi, M. Heidari, B. Azimi, C. Pevida, Development of novel waste tea-derived activated carbon promoted with sio_2 nanoparticles as highly robust and easily fluidizable sorbent for low-temperature co_2 capture, Journal of Environmental Chemical Engineering 11 (5) (10 2023). doi:10.1016/j.jece.2023.110437.

[46] R. Bakhtiari, S. Ghobadi, E. N. Güllüoğlu, L. I. Şanlı, S. A. Gürsel, E. Özden-Yenigün, Macroscopic assembly of flexible and strong green graphene fibres, RSC Advances 7 (43) (2017) 26735–26744. doi:10.1039/c7ra03975a.

[47] K. M. Keener, J. D. LaCrosse, J. K. Babson, Chemical method for determination of carbon dioxide content in egg yolk and egg albumen, Poultry Science 80 (7) (2001) 983–987. doi:10.1093/ps/80.7.983.
URL https://doi.org/10.1093/ps/80.7.983